INORGANIC CHEMISTRY FRONTIERS

RESEARCH ARTICLE

View Article Online
View Journal | View Issue

Check for updates

Cite this: *Inorg. Chem. Front.*, 2024, **11**, 5458

Cation and anion co-partial substitution induced centrosymmetric to noncentrosymmetric structural transformation to construct nonlinear-optical rare-earth oxythiogermanates†

Nan Zhang,[a] Mei Yang,[a] Wen-Dong Yao,[a] Wei Xu,[a] Wenfeng Zhou,[a] Wenlong Liu[a] and Sheng-Ping Guo *[a,b]

Received 13th May 2024,
Accepted 4th July 2024

DOI: 10.1039/d4qi01195c

rsc.li/frontiers-inorganic

Rational structural design and modification based on known compounds is an effective strategy to explore new nonlinear optical (NLO) materials. Here, three new rare-earth (RE) oxythiogermanates $Eu_{18}Ge_9O_5S_{31}$ (**1**), $Ca_{3.32}Eu_{14.68}Ge_9O_5S_{31}$ (**2**) and $Ba_3Eu_{15}Ge_9O_5S_{31}$ (**3**) were obtained by the novel cation and anion co-partial substitution strategy from the parent β-Eu_2GeS_4 (**0**), which induces centrosymmetric to noncentrosymmetric (NCS) structural transformation and NLO activities. They crystallize with a *pseudo*-zero dimensional structure in the chiral *R*3 space group, featuring almost linearly arranged isolated GeS_4 and $GeOS_3$ tetrahedra. Their optical band gaps were determined to be 2.18, 2.23 and 2.24 eV, respectively. **1** and **2** show balanced NLO properties with moderate second-harmonic generation (SHG) responses (0.5 and 0.6 × AGS) and high laser-induced damage thresholds (LIDTs) (3.3 × AGS). Moreover, theoretical calculations show that their NLO properties are determined by the synergistic effect of GeS_4 and $GeOS_3$ tetrahedra. This work enriches the chemistry of rarely studied RE oxychalcogenides and provides a fresh route for designing NCS structures targeting diverse applications.

Published on 16 July 2024. Downloaded on 2/18/2026 8:07:06 PM.

Introduction

Laser technology is one of the most important inventions after atomic energy, computers and semiconductors, and has been widely used in optical fiber communication, laser spectroscopy, laser radar and weapons, and laser scanning and ranging, however, the available laser sources are limited and need to be further explored.[1] In recent years, second-order nonlinear optical (NLO) materials have attracted much attention due to their second harmonic generation (SHG) ability.[2] Up to now, a large number of inorganic, organic, organometallic, inorganic–organic hybrid compounds, polymers and inorganic glass materials have been reported with SHG activities. There are already several commercial ultraviolet (UV), visible and near infrared (IR) NLO materials that can meet the practical requirements.[3] In contrast, the middle-IR NLO ones cannot meet the market's requirements.[4] Therefore, the exploration of novel middle-IR NLO ones is necessary while challenging.

Obtaining a noncentrosymmetric (NCS) crystal structure is the prerequisite condition for SHG activity. Over the past few decades, diverse methods have been introduced to design new NCS compounds to achieve this goal, which include but is not limited to (1) introduction of the typical MQ_4 (M = Al, Ga, In, Si, Ge, Sn, and P; Q = S and Se) tetrahedral functional motifs, which is the most widely used strategy and usually produces a large SHG effect;[5] (2) introduction of the d^{10} metal Zn, Cd, Hg, Cu or Ag, which can generate a high polar displacement in the coordination center, causing the asymmetric occupation of electrons in degenerate orbitals and distorting the molecular geometry;[6] (3) introduction of SOJT cations, including d^0 metal ions, Ti^{4+}, Zr^{4+}, Hf^{4+}, V^{5+}, Nb^{5+} and Ta^{5+};[7] (4) introduction of lone-pair cations, such as Pb^{2+}, Sb^{3+}, Sn^{2+}, As^{3+}, Bi^{3+}, Se^{4+}, Te^{4+}, I^{5+}, *etc.*;[8] (5) introduction of asymmetric π-conjugated planar triangular anion groups, such as BO_3^{3-}, CO_3^{2-}, NO_3^- and $C_3N_3O_3^{3-}$.[9] The above strategies are beneficial for obtaining NCS compounds with large SHG effects. As another important indicator, laser-induced damage threshold (LIDT) can be used to evaluate whether the materials can be used in high output power scenarios. In recent years, researchers have found that some mixed-anionic compounds

[a]*School of Chemistry and Chemical Engineering, Yangzhou University, Yangzhou, Jiangsu 225002, P. R. China. E-mail: spguo@yzu.edu.cn, spguo@ynu.edu.cn*
[b]*Yunnan Key Laboratory of Electromagnetic Materials and Devices, National Center for International Research on Photoelectric and Energy Materials, School of Materials and Energy, Yunnan University, Kunming, Yunnan 650091, P. R. China*

†Electronic supplementary information (ESI) available: Additional tables and pictures. CCDC 2329237–2329239. For ESI and crystallographic data in CIF or other electronic format see DOI: https://doi.org/10.1039/d4qi01195c

This journal is © the Partner Organisations 2024

Published on 16 July 2024. Downloaded on 2/18/2026 8:07:06 PM.

can achieve a good balance between a large SHG effect and a high LIDT, and most of them crystallize with low-dimensional structures, which is conducive to improving the polarizability and NLO coefficient (d_{eff}).[10] At the same time, hybridization occurs between the anionic orbitals of different elements in the structure, resulting in their relatively stable physicochemical properties.

Anion partial substitution (APS) based on known NCS or centrosymmetric (CS) structures has been proven to be a useful method for achieving mixed-anionic compounds. For example, new NCS oxyselenide $SrGeOSe_2$ ($P2_12_12_1$) was obtained by the isovalent APS method using $SrGeO_3$ ($C2/c$) as the template,[11] and aliovalent APS of $SnBr_2$ ($P6_3/m$) realizes the CS-to-NCS structural change to obtain $Sn_7Br_{10}S_2$ ($P6_3$).[8] Moreover, the SHG response of $Ag_2In_2SiS_{3.06}Se_{2.94}$ (1.1 × AGS) is enhanced more than 3 times that of its template $Ag_2In_2SiS_6$ (0.3 × AGS) after S sites are partially substituted by the heavier congener Se.[12] It is worth noting that the mixed-anionic groups in the above compounds have a large degree of distortion, so the birefringence (Δn) increases to realize phase-matching (PM). These studies indicate that the APS strategy can not only achieve structural transformation, but also be an effective route for simultaneously optimizing the d_{eff} and Δn. In addition to APS, cation partial substitution (CPS) is also a useful method for achieving CS-to-NCS structural transformation. Successful cases include $(K_{0.38}Ba_{0.81})Ga_2Se_4$,[13] $(Na_3Rb)Hg_2Ge_2S_8$ [14] and $K_2Ag_3Sb_3S_7$,[15] which can be obtained from the parent $BaGa_2Se_4$, $Rb_4Hg_2Ge_2S_8$ and $K_2Sb_4S_7$, respectively. However, as far as we know, hitherto there is no report about designing NLO materials using the cation and anion co-partial substitution (CAPS) strategy.

Guided by the above considerations, three novel RE oxythiogermanates $M_xEu_{18-x}Ge_9O_5S_{31}$ (M = Ca, x = 0, 3.32; M = Ba, x = 3) could be obtained by the CAPS method by taking β-Eu_2GeS_4 (**0**) as the structural template after much effort (Fig. S1†).[16]

Experimental section

Syntheses

$Eu_{18}Ge_9O_5S_{31}$ (**1**), $Ca_{3.32}Eu_{14.68}Ge_9O_5S_{31}$ (**2**) and $Ba_3Eu_{15}Ge_9O_5S_{31}$ (**3**) were synthesized *via* a solid-state method. Eu (Aladdin, 99.95%), CaO (Macklin, 99.5%), Ba (Aladdin, 99.9%), GeO_2 (Macklin, 99.9%), Ge (Aladdin, 99.999%), and S (Aladdin, 99.9%) were used directly without any purification. Single crystals of **1–3** could be obtained using the molar ratios of Eu : Ge : GeO_2 : S = 18 : 6 : 3 : 31, Eu : CaO : Ge : S = 14 : 4 : 9 : 31 and Eu : Ba : Ge : GeO_2 : S = 15 : 3 : 6 : 3 : 31, with a total mass of 500 mg, and 400 mg KI was used as flux. The mixtures were ground into fine powder using an agate mortar, then pressed into pellets, and further loaded into fused silica tubes. The tubes were evacuated to a high vacuum of 1×10^{-4} Torr and flame-sealed, and then were heated to 1173 K for 20 h in a muffle furnace, and maintained at 1173 K for two days. Finally, the reaction was cooled down to room temperature within five days, and the crystals **1** and **2** (Fig. S1†) were obtained in a yield of 70% based on Eu, while the yield of **3** was really very low although many attempts were made to optimize the synthesis; crystals **1–3** are stable under atmospheric conditions.

Powder X-ray diffraction (PXRD) patterns were collected with a Bruker D8 Advance diffractometer at 40 kV and 100 mA using Cu-Kα radiation (λ = 1.5406 Å) with a scan speed of 5° min^{-1} at room temperature. The simulated patterns were generated with the Mercury v3.8 program provided by the CCDC and single-crystal reflection data. The experimental and simulated PXRD patterns (Fig. S2†) match well, suggesting that the obtained samples are pure. Semiquantitative microscopic elemental analysis of the as-prepared single crystals of **1–3** was performed using a field-emission scanning electron microscope (FESEM, HITACHI S-4800II) equipped with an energy dispersive X-ray spectroscope (EDS, Bruker, Quantax), which confirms the presence of Eu, Ge and S in **1**, and Eu, Ca/Ba, Ge, and S in **2** and **3**. The content of O is not considered as the measurement process has an important influence on its value (Fig. S3†).

Structure determination

The single crystal X-ray diffraction data of **1–3** were collected on a Bruker D8 QUEST X-ray diffractometer with Mo-Kα radiation (λ = 0.71073 Å) at room temperature. Whereafter, the single-crystal structures were solved by Direct Methods and refined by full-matrix least-squares techniques on F^2 with aeolotropic thermal parameters for all atoms using SHELXL within the Olex2 interface.[17] The final refinement also included a secondary extinction correction. The crystal data and structural refinement information are summarized in Table S1.† Atomic coordinates and equivalent isotropic displacement parameters, and bond distances are provided in Tables S2 and S3,† respectively. The CIF documents of **1–3** are also deposited with the CCDC numbers 2329237–2329239.†

Infrared and diffuse reflectance spectroscopies

The IR spectra between 400 and 4000 cm^{-1} (2.5–25 μm) were recorded on a VERTEX 70 FT-IR spectrophotometer, in which KBr was used as the reference. A computer-controlled Varian Cary 5000 UV-vis-NIR spectrometer in the wavelength range of 200–1600 nm was used to record the diffuse reflectance spectra of **1–3**. The reference was a $BaSO_4$ plate and the finely ground powdery sample was coated. The absorption spectra were obtained from the reflection spectra using the Kubelka–Munk function.[18]

Second-harmonic generation (SHG) measurement

Size-dependent SHG measurement for the powder samples of **1** and **2** was carried out using a 2.1 μm laser as the radiation source using the modified Kurtz–Perry powder method.[19] The samples were sieved into several different particle size ranges (25–45, 45–75, 75–110, 110–150, 150–200, and 200–250 μm), and benchmark AGS samples with the same particle size ranges were used as the standards. The intensity of the frequency-doubled output signal produced from a photomultiplier tube was recorded using a digital oscilloscope.

Published on 16 July 2024. Downloaded on 2/18/2026 8:07:06 PM.

Laser-induced damage threshold (LIDT) measurement

The LIDTs for the 75–110 μm powder samples of **1–3** and reference AGS were measured with a 1064 nm laser as radiation light using the single-pulse method.[20,21] The pulse width τp and repetition were set to 10 ns and 1 Hz, respectively. The power of the light source E was continuously increased until the spot area appeared. According to the formula: I(threshold) = $E/(S\tau p)$, where S indicates the damage spot area.

Thermal expansion anisotropy (TEA)

The variations of lattice parameters of **1** and **2** depending on the temperature from 100 to 400 K with a step of 20 K were determined from *in situ* X-ray diffraction measurements. Thermal expansion coefficients (TECs, $\alpha L = R_0^{-1}\,[\mathrm{d}R(T)/\mathrm{d}T]$, where R_0 is the a, b or c value at $T = 0$ K, and a, b and c are the axis lengths) of the lattice parameters of **1** and **2** were derived. The thermal expansion anisotropy (TEA) values of **1** and **2** were calculated according to the equation TEA = $|\alpha L_{\max}/\alpha L_{\min}|$.[22] The TEA of reference AGS was calculated in the same way and the value is similar to other reported ones.

Birefringence measurement

The birefringences for crystalline samples of **1–3** were measured with a polarizing microscope. The wavelength of the light source was 546 nm. The birefringence was calculated according to the equation ΔR (retardation) = $|N_e - N_o| \times T = \Delta n \times T$, where ΔR denotes the optical path difference, Δn represents the birefringence, and T is the thickness of the crystal.

Thermal analysis

A Labsys™ TG-DTA16 (SETARAM) thermal analyzer was used to investigate the thermal properties using differential scanning calorimetric (DSC) analysis (the DSC instrument was calibrated with Al_2O_3). About 20 mg samples of **1** and **2** were placed in a silica tube (5 mm o.d. × 3 mm i.d.) and subsequently sealed under high vacuum. The heating and the cooling rates were both 15 K min^{-1}. To verify the phases, samples **1** and **2** were sealed in vacuum quartz tubes and then heated to 1000 °C in a muffle oven, respectively. After being kept at the corresponding temperatures for 1 day and then quenched to room temperature, the samples were analyzed using the PXRD technique.

Theoretical calculations

First-principles density functional theory calculations of **1–3** were performed using the CASTEP package in Material Studio software.[23] The Perdew–Burke–Ernzerhof generalized gradient approximation was employed for the exchange and correlation function.[24] The norm-conserving pseudopotentials of Eu, Ca, Ba, Ge, O and S consider 6s5d4f, 4s, 6s, 4s4p, 2s2p and 3s3p orbitals as the valence states, respectively. The L(S)DA+U method was used to treat the strongly correlated 4f electrons. A plane-wave cutoff energy of 830 eV and a threshold of 5×10^{-7} eV per atom were set for the self-consistent-field convergence of the total electronic energy. A 2 × 2 × 2 Monkhorst–Pack k-point grid in the BZ of the primitive cell was chosen.

The optical properties including the dielectric function, second-order susceptibilities, and refractive index n were calculated using the same method used in our previous studies.[25,26]

Results and discussion

Crystal structures

As the parent of **1–3**, **0** crystallizes in the monoclinic space group $P2_1/m$ (no. 11), and there are two Eu, one Ge and three S atoms in the crystallographically independent unit (Fig. S4†).[16] Each Eu is coordinated with eight S atoms to form the EuS_8 bicapped trigonal prism (*btp*) with the Eu–S bond distances of 2.951(3)–3.533(1) Å, and each Ge is fourfold-coordinated with S atoms to form a GeS_4 tetrahedron with the Ge–S bond distances of 2.190(2)–2.195(2) Å, and all the GeS_4 units in the structure are centrosymmetrically arranged in the reverse way, resulting in the cancellation of microscopic second-order polarizability (Fig. 1a and c).

1–3 crystallize in the space group $R3$ (no. 146) of the trigonal system. There are six M, five Ge, three O and eleven S atoms in the crystallographically independent unit. The occupation of six M sites is complex, and the details are as follows: completely occupied by Eu (in **1**); five M sites are co-occupied by Eu and Ca, and the sixth one is completely occupied by Eu (in **2**); five M sites are completely occupied by Eu, and one is completely occupied by Ba (in **3**) (Fig. S5†). Only the structure of **1** is described here in detail considering their structural similarity. The six Eu atoms are coordinated with seven or eight O/S atoms to form three $EuOS_6$ (Eu1, Eu2 and Eu5) mono-capped trigonal prisms (*mtps*), two $EuOS_7$

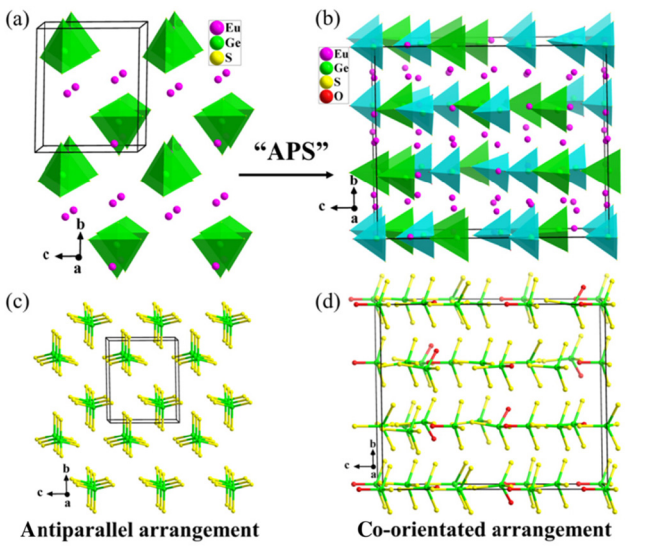

Fig. 1 Crystal structures of **0** (a) and **1** (b); blue and green tetrahedra represent $GeOS_3$ and GeS_4 units, respectively; (c) alignment of GeS_4 tetrahedra in **0**; (d) alignment of GeS_4 and $GeOS_3$ tetrahedra in **1**. The Eu–S and Eu–O bonds are omitted for clarity.

This journal is © the Partner Organisations 2024

Published on 16 July 2024. Downloaded on 2/18/2026 8:07:06 PM.

(Eu3, Eu4) *btps*, and a EuS_8 (Eu6) *btp*, respectively. All the five Ge atoms are tetracoordinated to form distorted tetrahedra. Differently, Ge2 and Ge3 only coordinate with S atoms, while Ge1, Ge4 and Ge5 bond with one O and three S atoms. When the Eu–S and Eu–O bonds are omitted, the structure of **1** is *pseudo*-zero-dimensional (0D) since all the tetrahedral units are isolated (Fig. 1b), which is similiar to the first quaternary SHG active RE oxythiogermanate Eu_3GeOS_4.[27] However, all Ge atoms in Eu_3GeOS_4 coordinate with one O and three S atoms to form $GeOS_3$ tetrahedra, and their arrangement does not tend in exactly the same direction, which results in a much weaker SHG response than those of **1** and **2**. The Eu–S bond length ranging from 2.8952(18) to 3.4314(19) Å is comparable to 2.9115(15)–3.1827(16) Å in Eu_3GeOS_4. The Eu–O distances range from 2.423(3) to 2.623 (5) Å, which is reasonable when compared with 2.330(5)–2.801(7) Å in $Eu_9MgS_2B_{20}O_{41}$.[28] The Ge–S and Ge–O bond lengths show distances of 2.2086(19)–2.225(2) and 1.789(5)–1.806(8) Å, close to 2.2739(7) and 1.735(2)–1.8586(14) Å in $La_3Ga_3Ge_2S_3O_{10}$,[29] respectively.

From structures **0** to **1**, the APS strategy was performed and 5/36 of the S atoms could be replaced with O atoms, which breaks the centrosymmetry of **0** and generates the NLO activity of **1** (Fig. 1b and d). In its structure, isolated GeS_4 and $GeOS_3$ tetrahedra are almost parallelly aligned, leading to a superposition of microscopic SHG coefficients and further macroscopically enhanced NLO effects. In addition, from **0** to **2** and **3**, the CAPS method was used. The structural transition from **0** to **1–3** is reflected from centrosymmetric $P2_1/m$ to chiral $R3$, which shows that the CAPS method results in the space group transition from low symmetry to high symmetry, with the change of direction and distortion for anion groups. Therefore, this study establishes a fresh strategy for the further exploration of NLO materials.

Optical properties

The UV-vis-NIR diffuse reflectance spectra show optical band gap values of 2.18, 2.23 and 2.24 eV for **1–3** (Fig. 2a), which match well with their red crystal color. Notably, **2** and **3** have larger optical band gaps than **1**, which may be because Eu in **1** is partially replaced by alkaline earth metals Ca and Ba, respectively, thus avoiding the negative effects of d–d or f–f transitions. Therefore, it can be inferred that the band gap value will be further improved when Eu is completely replaced by Ca and Ba, thus further increasing the LIDTs. The FT-IR spectra of **1–3** (Fig. 2b) show only one absorption peak (about 640 cm^{-1}), which belongs to the Ge–O stretching mode.[30] Based on the above data, the transparency ranges for the powder samples of **1–3** are 0.6–15.6 μm, covering the two critical atmospheric windows (3–5 and 8–12 μm).

Birefringence measurements of **1–3** show that their optical path differences are 0.672, 1.009 and 0.466 μm with crystal thicknesses of 8.96, 18.56 and 16.51 μm (Fig. S6†). Their birefringences are determined to be 0.0749, 0.0543 and 0.0282, respectively,[33] and values of **1** and **2** are ideal ones for achieving phase matching, consistent with their experimental PM behaviors.

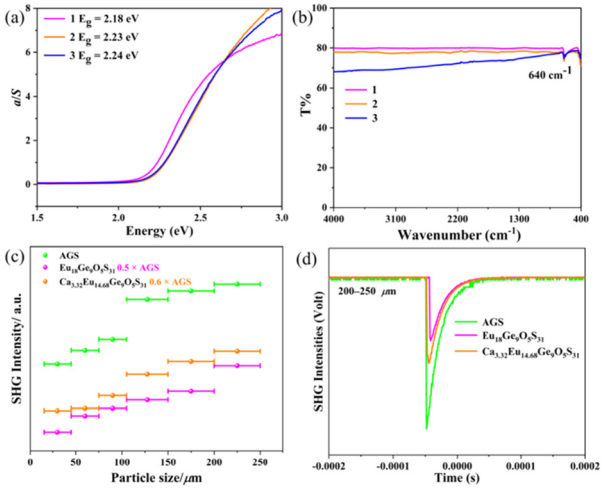

Fig. 2 (a) The UV–vis–NIR diffuse reflection and (b) IR spectra of **1–3**; (c) size-dependent SHG responses and (d) SHG intensities at 200–250 μm of **1**, **2** and AGS under 2.1 μm laser radiation.

SHG and LIDT properties

Considering the chiral structures of **1–3**, their SHG responses were measured using the Kurtz–Perry technique under a 2.1 μm laser. Only the NLO behaviors of **1** and **2** are discussed here since the amount of sample **3** is not enough for further testing. Both **1** and **2** exhibit PM behaviors (Fig. 2c), evidenced by the increasing SHG responses along with the increased particle sizes. Their 200–250 μm samples show the SHG responses of 0.5 and 0.6 × AGS, respectively (Fig. 2d), which are large enough from the view point of application.[31]

The 75–110 μm powder samples of **1**, **2** and AGS were measured under a 1064 nm laser to evaluate their LIDTs (Table S4†). Both **1** and **2** exhibit large LIDT values (11.44 MW cm^{-2}), which are 3.3 times that of AGS (3.48 MW cm^{-2}). In addition to the band gap, thermal expansion anisotropy (TEA), chemical composition, lattice dynamics and crystal quality can also influence the LIDT. Therefore, TEA tests were performed on **1** and **2** to further judge their application potential under high frequency lasers (Fig. 3a–d). The smaller TEA values of **1** (2.58) and **2** (1.94) than that of AGS (2.97) confirm that **1** and **2** have larger LIDT values since NLO materials with smaller TEA values may withstand greater thermal shock (Table S5†).[32] The increased LIDT values overcome the application limitation of benchmark AGS and improve the possibility of using them in scenarios with a high output power. To date, there are rare studies on rare-earth oxychalcogenides as NLO materials. Most of them exhibit relatively weak SHG responses (< 0.5 × AGS) (Table S6†). The acceptable SHG intensity and enhanced LIDTs reveal that **1** and **2** are new promising MIR NLO materials, which enrich the system of rare-earth oxychalcogenide NLO matreials.

Published on 16 July 2024. Downloaded on 2/18/2026 8:07:06 PM.

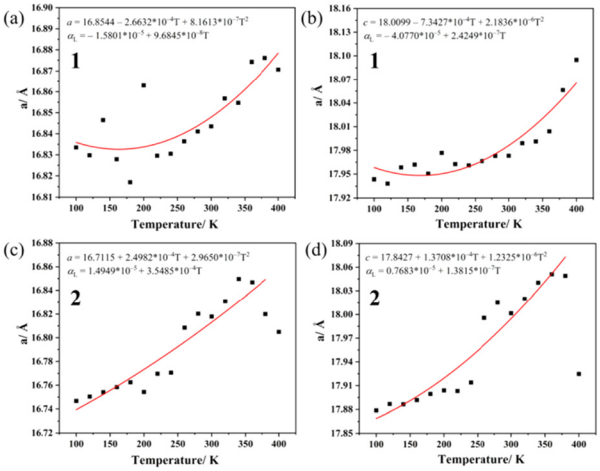

Fig. 3 Temperature-dependent lattice parameters' variation for *a*/Å and *c*/Å of **1** (a and b) and **2** (c and d), respectively.

Thermal analysis

Both the heating and cooling processes for the DSC curves of **1** and **2** show a peak (Fig. S7†). The experimental PXRD patterns after calcination are compared with standard cards in Jade, and the results indicate that sample **1** decomposes into Eu_2GeS_4 and Eu_2O_2S, and **2** decomposes into Eu_2GeS_4, CaO and Eu_2O_2S at 970 and 997 °C, respectively (Fig. S8†). Their high thermal stability is comparable to those of the rising benchmark IR NLO material $BaGa_4Se_7$ (melting point: ~968 °C)[34] and the benchmark AGS (melting point: ~1000 °C).

Theoretical calculations

First-principles calculations with the CASTEP package were carried out on **1–3** to explore the structure–property relationship.[23] Their band gaps were calculated to be 2.60, 2.62 and 2.65 eV, respectively, which are reasonable compared with the experimental ones. The top of valence band (VB) and the bottom of conduction band (CB) are located at the same *k* point, indicating direct band gaps of **1–3** (Fig. 4a, c and e). The calculated total and partial densities of states (TDOS and PDOS) of **1–3** show that the VB from −4 to −0 eV is almost constituted of Eu 4f and S 3p orbitals, and the CB is primarily from the contribution of Eu 5d orbitals between 2 and 10 eV (Fig. 4b, d and f). As a result, electronic transition between Eu 4f and Eu 5d orbitals determines their band gaps. In addition, the SHG coefficients of **1–3** were calculated to further understand their NLO behaviors (Fig. S9a, S9c and S9e†). The space group *R*3 belongs to point group 3 and has six non-vanishing SHG tensors (χ_{11}, χ_{14}, χ_{15}, χ_{22}, χ_{31}, and χ_{33}), of which only four are independent (χ_{11}, χ_{15}, χ_{22}, and χ_{33}) under the restriction of Kleinman's symmetry. The corresponding NLO coefficients d_{11}, d_{15}, d_{22}, and d_{33} of **1–3** were calculated to be 3.21, 3.10, 3.10, and 2.90 pm V^{-1}, respectively. The calculated values are smaller than the experimental ones, which may be due to differences between the computational model and actual crystals. The calculated Δn values of **1–3** are 0.04, 0.03 and 0.02, respectively, which are consistent with the experimental values and match the PM behaviors of **1** and **2** (Fig. S9b, S9d and S9f†).

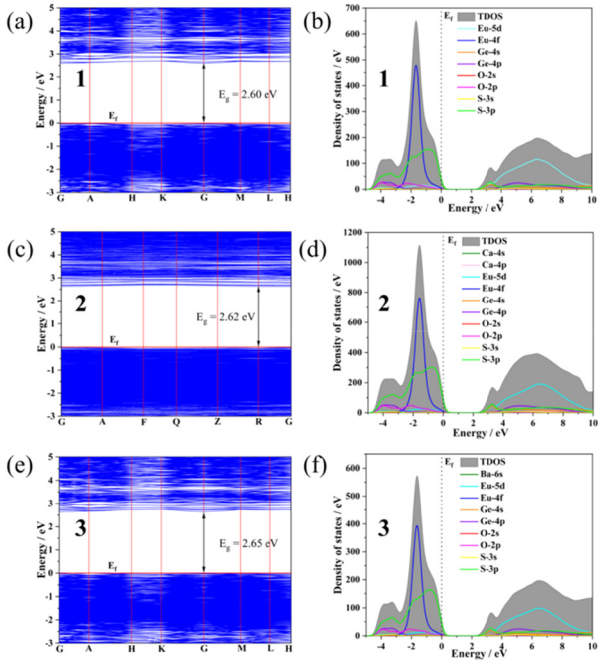

Fig. 4 The calculated band structures (a, c, and e) and density of states (b, d, and f) of **1–3**.

To explore the origin of SHG effects, the dipole moments of $GeOS_3$ and GeS_4 tetrahedra in one unit for **1** and **2** were calculated, which are 0.085 and 0.116 esu cm $Å^{-3}$ in **1** and 0.096 and 0.120 esu cm $Å^{-3}$ in **2** (Table S7†), respectively. Obviously, $GeOS_3$ tetrahedra have a larger SHG contribution than GeS_4 tetrahedra. As shown in Fig. S10,† the dipole moments of GeS_4 and $GeOS_3$ point almost in the same direction, resulting in the superposition of the microscopic second-order polarizability. Moreover, the distortion degrees of $GeOS_3$ and GeS_4 units in **1** and **2** were calculated according to their bond lengths, bond angles and side lengths. The results indicate that the anionic groups in **2** have larger distortion degrees than those in **1** (Table S8†). The anion groups GeS_4 and $GeOS_3$ have a dipole moment vector angle of 15.01° in **1**, while in **2**, anion groups have a more linear arrangement and the dipole moment vector angle is only 2.696°. The larger distortion in **2** and the more linear arrangement of anion groups lead to its higher SHG response than that in **1**, suggesting that partial substitution of Eu with Ca is conducive to the NLO properties.

Conclusion

In summary, three new rare earth oxythiogermanates were synthesized *via* the novel CAPS strategy, which not only realizes the CS-to-NCS structural transformation, but also produces satisfactory SHG activities, *viz.* enough SHG responses, enhanced LIDTs, wide IR transparent regions, moderate birefringences and high thermal stability. This work provides a new ideal for

 This journal is © the Partner Organisations 2024

designing high-performance IR NLO candidates, and also opens a new avenue (RE oxychalcogenides) for potential IR NLO material systems.

Data availability

The data supporting this article have been included as part of the ESI.†

Crystallographic data for **1–3** has been deposited with the CCDC numbers 2329237–2329239.†

Conflicts of interest

The authors declare no competing financial interests.

Acknowledgements

The authors acknowledge the financial support from the National Natural Science Foundation of China (22071212 and 22371246) and the Natural Science Foundation of Yunnan Province (202401AS070120).

References

1 (*a*) T. Kojima, S. Konno, S. Fujikawa, K. Yasui, K. Yoshizawa, Y. Mori, T. Sasaki, M. Tanaka and Y. Okada, 20-W ultraviolet-beam generation by fourth-harmonic generation of an all-solid-state laser, *Opt. Lett.*, 2000, **25**, 58–60; (*b*) H. C. Lu, R. Gautier, M. D. Donakowski, T. T. Tran, B. W. Edwards, J. C. Nino, P. S. Halasyamani, Z. T. Liu and K. R. Poeppelmeier, Nonlinear Active Materials: An Illustration of Controllable Phase Matchability, *J. Am. Chem. Soc.*, 2013, **135**, 11942–11950.

2 (*a*) C. T. Chen and G. Z. Liu, Recent Advances in Nonlinear Optical and Electro-Optical Materials, *Annu. Rev. Mater. Sci.*, 1986, **16**, 203–243; (*b*) D. Burland, Optical Nonlinearities In Chemistry: Introduction, *Chem. Rev.*, 1994, **94**, 1–2; (*c*) W. F. Zhou and S. P. Guo, Rational Design of Novel Promising Infrared Nonlinear Optical Materials: Structural Chemistry and Balanced Performances, *Acc. Chem. Res.*, 2024, **57**, 648–660.

3 (*a*) T. T. Tran, H. W. Yu, J. M. Rondinelli, K. R. Poeppelmeier and P. S. Halasyamani, Deep Ultraviolet Nonlinear Optical Materials, *Chem. Mater.*, 2016, **28**, 5238–5258; (*b*) C. Wu, G. Yang, M. G. Humphrey and C. Zhang, Recent advances in ultraviolet and deep-ultraviolet second-order nonlinear optical crystals, *Coord. Chem. Rev.*, 2018, **375**, 459–488.

4 S. P. Guo, Y. Chi and G. C. Guo, Recent achievements on middle and far-infrared second-order nonlinear optical materials, *Coord. Chem. Rev.*, 2017, **335**, 44–57.

5 G. M. Li, K. Wu, Q. Liu, Z. H. Yang and S. L. Pan, $Na_2ZnGe_2S_6$: A New Infrared Nonlinear Optical Material with Good Balance between Large Second-Harmonic Generation Response and High Laser Damage Threshold, *J. Am. Chem. Soc.*, 2016, **138**, 7422–7428.

6 (*a*) H. Chen, W. B. Wei, H. Lin and X. T. Wu, Transition-metal-based chalcogenides: A rich source of infrared nonlinear optical materials, *Coord. Chem. Rev.*, 2021, **448**, 214154; (*b*) A. Yelisseyev, S. Lobanov, M. Molokeev, S. Z. Zhang, A. Pugachev, Z. S. Lin, V. Vedenyapin, A. Kurus, A. Khamoyam and L. Isaenko, A New Nonlinear Optical Selenide Crystal $AgLiGa_2Se_4$ with Good Comprehensive Performance in Mid-Infrared Region, *Adv. Opt. Mater.*, 2021, **9**, 2001856.

7 J. Chen, C. L. Hu, X. H. Zhang, B. X. Li, B. P. Yang and J. G. Mao, $CsVO_2F(IO_3)$: An Excellent SHG Material Featuring an Unprecedented 3D $[VO_2F(IO_3)]^-$ Anionic Framework, *Angew. Chem., Int. Ed.*, 2020, **59**, 5381–5384.

8 (*a*) H. W. Yu, J. Young, H. P. Wu, W. G. Zhang, J. M. Rondinelli and P. S. Halasyamani, Electronic, Crystal Chemistry, and Nonlinear Optical Property Relationships in the Dugganite $A_3B_3CD_2O_{14}$ Family, *J. Am. Chem. Soc.*, 2016, **138**, 4984–4989; (*b*) X. H. Li, Z. H. Shi, M. Yang, W. L. Liu and S. P. Guo, $Sn_7Br_{10}S_2$: The First Ternary Halogen-Rich Chalcohalide Exhibiting a Chiral Structure and Pronounced Nonlinear Optical Properties, *Angew. Chem., Int. Ed.*, 2022, **61**, e202115871.

9 X. H. Meng, P. F. Gong, C. L. Tang, W. L. Yin, Z. S. Lin and M. J. Xia, From Centrosymmetry to Noncentrosymmetry: Tailoring the Structural Arrangements of Carbonates with Strong Nonlinear Optical Response through Partial Anion Substitution, *Adv. Opt. Mater.*, 2021, **9**, 2100594.

10 J. J. Xu and K. Wu, Comprehensive review on multiple mixed-anion ligands, physicochemical performances and application prospects in metal oxysulfides, *Coord. Chem. Rev.*, 2023, **486**, 215139.

11 M. Y. Ran, Z. J. Ma, H. Chen, B. X. Li, X. T. Wu, H. Lin and Q. L. Zhu, Partial Isovalent Anion Substitution to Access Remarkable Second-Harmonic Generation Response: A Generic and Effective Strategy for Design of Infrared Nonlinear Optical Materials, *Chem. Mater.*, 2020, **32**, 5890–5896.

12 J. Li, W. F. Zhou, W. D. Yao, W. L. Liu and S. P. Guo, Three-in-One Tetrahedral Functional Units Constructing Diamondlike $Ag_2In_2SiS_{3.06}Se_{2.94}$ with High-Performance Nonlinear-Optical Activity, *Inorg. Chem.*, 2023, **62**, 13179–13183.

13 Y. N. Li, Y. Chi, Z. D. Song, H. G. Xue, N. T. Suen and S. P. Guo, Partial substitution induced centrosymmetric to noncentrosymmetric structure transformation and promising second-order nonlinear optical properties of $(K_{0.38}Ba_{0.81})Ga_2Se_4$, *Chem. Commun.*, 2019, **55**, 13701–13704.

14 C. L. Tang, W. H. Xing, F. Liang, M. R. Sun, J. Tang, Z. S. Lin, J. Y. Yao, K. X. Chen, J. Y. Wu, W. L. Yin and B. Kang, Structural modification from centrosymmetric $Rb_4Hg_2Ge_2S_8$ to noncentrosymmetric $(Na_3Rb)Hg_2Ge_2S_8$: mixed alkali metals strategy for infrared nonlinear optical material design, *J. Mater. Chem. C*, 2022, **10**, 3300–3306.

Published on 16 July 2024. Downloaded on 2/18/2026 8:07:06 PM.

Published on 16 July 2024. Downloaded on 2/18/2026 8:07:06 PM.

15 C. Liu, S. H. Zhou, Y. Xiao, C. Zhang, H. Lin and Y. Liu, Aliovalent-cation-substitution-induced structure transformation: a new path toward high-performance IR nonlinear optical materials, *J. Mater. Chem. C*, 2021, **9**, 15407–15414.

16 M. Tampier and D. Johrendt, Structural Evidence for Ferroelectricity in Eu_2GeS_4, *J. Solid State Chem.*, 2001, **158**, 343–348.

17 O. V. Dolomanov, L. J. Bourhis, R. J. Gildea, J. A. K. Howard and H. Puschmann, OLEX2: A Complete Structure Solution, Refinement and Analysis Program, *J. Appl. Crystallogr.*, 2009, **42**, 339–341.

18 (*a*) W. W. Wendlandt and H. G. Hecht, *Reflectance Spectroscopy*, Interscience Publishers, New York, 1966; (*b*) G. Kortüm, *Reflectance Spectroscopy*, Springer, 1969.

19 S. K. Kurtz and T. T. Perry, A Powder Technique for the Evaluation of Nonlinear Optical Materials, A Powder Technique for the Evaluation of Nonlinear Optical Materials, *J. Appl. Phys.*, 1968, **39**, 3798–3813.

20 M. J. Zhang, X. M. Jiang, L. J. Zhou and G. C. Guo, Two phases of Ga_2S_3: promising infrared second-order nonlinear optical materials with very high laser induced damage thresholds, *J. Mater. Chem. C*, 2013, **1**, 4754–4760.

21 M. M. Chen, Z. J. Ma, B. X. Li, W. B. Wei and X. T. Wu, $M_2As_2Q_5$ (M = Ba, Pb; Q = S, Se): a source of infrared nonlinear optical materials with excellent overall performance activated by multiple discrete arsenate anions, *J. Mater. Chem. C*, 2021, **9**, 1156–1163.

22 Q.-T. Xu, S.-S. Han, J.-N. Li and S.-P. Guo, $NaGa_3Se_5$: An Infrared Nonlinear Optical Material with Balanced Performance Contributed by Complex $\{[Ga_3Se_5]^-\}_\infty$ Anionic Network, *Inorg. Chem.*, 2022, **61**, 5479–5483.

23 S. J. Clark, M. D. Segall, C. J. Pickard, P. J. Hasnip, M. I. J. Probert, K. Refson and M. C. Payne, First principles methods using CASTEP, *Z. Kristallogr. – Cryst. Mater.*, 2005, **220**, 567–570.

24 J. P. Perdew and K. Burke, Generalized Gradient Approximation Made Simple, *Phys. Rev. Lett.*, 1996, **77**, 3865.

25 X. Huang, S. H. Yang, X. H. Li, W. L. Liu and S. P. Guo, $Eu_2P_2S_6$: The First Rare-Earth Chalcogenophosphate Exhibiting Large Second-Harmonic Generation Response and High Laser-Induced Damage Threshold, *Angew. Chem., Int. Ed.*, 2022, **61**, e202206791.

26 S. P. Guo, X. Y. Cheng, Z. D. Sun, Y. Chi, B. W. Liu, X. M. Jiang, S. F. Li, H. G. Xue, S. Q. Deng, V. Duppel, J. Köhler and G. C. Guo, Large Second Harmonic Generation (SHG) Effect and High Laser-Induced Damage Threshold (LIDT) Observed Coexisting in Gallium Selenide, *Angew. Chem., Int. Ed.*, 2019, **58**, 8087–8091.

27 M. Yang, W. D. Yao, W. L. Liu and S. P. Guo, The first quaternary rare-earth oxythiogermanate with second-harmonic generation and ferromagnetic behavior, *Chem. Commun.*, 2023, **59**, 3894–3897.

28 Y. Chi, J. Xu, H. G. Xue, Y. P. Zhang, X. L. Chen, M. H. Whangbo, S. P. Guo and S. Q. Deng, Triple-Kagomé-Layer Slabs of Mixed-Valence Rare-Earth Ions Exhibiting Quantum Spin Liquid Behaviors: Synthesis and Characterization of $Eu_9MgS_2B_{20}O_{41}$, *J. Am. Chem. Soc.*, 2019, **141**, 9533–9536.

29 H. Yan, Y. Matsushita, K. Yamaura and Y. Tsujimoto, $La_3Ga_3Ge_2S_3O_{10}$: An Ultraviolet Nonlinear Optical Oxysulfide Designed by Anion-Directed Band Gap Engineering, *Angew. Chem., Int. Ed.*, 2021, **60**, 26561–26565.

30 B. W. Liu, X. M. Jiang, G. E. Wang, H. Y. Zeng, M. J. Zhang, S. F. Li, W. H. Guo and G. C. Guo, Oxychalcogenide $BaGeOSe_2$: Highly Distorted Mixed-Anion Building Units Leading to a Large Second-Harmonic Generation Response, *Chem. Mater.*, 2015, **27**, 8189–8192.

31 L. Kang, M. L. Zhou, J. Y. Yao, Z. S. Lin, Y. C. Wu and C. T. Chen, Metal Thiophosphates with Good Mid-infrared Nonlinear Optical Performances: A First-Principles Prediction and Analysis, *J. Am. Chem. Soc.*, 2015, **137**, 13049–13059.

32 S. F. Li, X. M. Jiang, B. W. Liu, D. Yan, C. S. Lin, H. Y. Zeng and G. C. Guo, Superpolyhedron-Built Second Harmonic Generation Materials Exhibit Large Mid-Infrared Conversion Efficiencies and High Laser-Induced Damage Thresholds, *Chem. Mater.*, 2017, **29**, 1796–1804.

33 W. L. Xie, F. M. Li, J. B. Chen, Z. H. Yang, G. M. Li and S. L. Pan, Improved Birefringence Activated by Tetrahedra Decorated with a Single Linear Unit, *Angew. Chem., Int. Ed.*, 2023, **62**, e202307895.

34 J. Y. Yao, D. J. Mei, L. Bai, Z. S. Lin, W. L. Yin, P. Z. Fu and Y. C. Wu, $BaGa_4Se_7$: A New Congruent-Melting IR Nonlinear Optical Material, *Inorg. Chem.*, 2010, **49**, 9212–9216.

 This journal is © the Partner Organisations 2024